

JGR Solid Earth

RESEARCH ARTICLE

10.1029/2018JB017050

Seismicity-Scanning Based on Navigated Automatic Phase-Picking

Fengzhou Tan^{1,2} , Honn Kao^{1,2} , Edwin Nissen¹ , and David Eaton³ 

¹School of Earth and Ocean Sciences, University of Victoria, Victoria, British Columbia, Canada, ²Geological Survey of Canada, Pacific Geoscience Centre, Sidney, British Columbia, Canada, ³Department of Geoscience, University of Calgary, Calgary, Alberta, Canada

Key Points:

- We take a cocktail approach combining merits of three different techniques to delineate complex spatiotemporal distribution of seismicity
- This new method, named Seismicity-Scanning based on Navigated Automatic Phase-picking (S-SNAP), is comprehensive, accurate, and automated
- In case study using dense array data, it located about 3 times more events than a template matching method without any false detections

Correspondence to:

F. Tan,
ftan@uvic.ca

Citation:

Tan, F., Kao, H., Nissen, E., & Eaton, D. (2019). Seismicity-Scanning based on Navigated Automatic Phase-picking. *Journal of Geophysical Research: Solid Earth*, 124, 3802–3818. <https://doi.org/10.1029/2018JB017050>

Received 16 NOV 2018

Accepted 23 MAR 2019

Accepted article online 31 MAR 2019

Published online 6 APR 2019

Abstract We propose a new method, named Seismicity-Scanning based on Navigated Automatic Phase-picking (S-SNAP), that is capable of delineating complex spatiotemporal distributions of seismicity. This novel algorithm takes a cocktail approach that combines source scanning, kurtosis-based phase picking, and the maximum intersection location technique into a single integrated workflow. This method is automated, detecting and locating earthquakes efficiently, comprehensively, and accurately. We apply S-SNAP to a data set recorded by a dense local seismic array during a hydraulic fracturing operation to test this novel approach and to demonstrate its effectiveness in relation to existing methods. Overall, S-SNAP found about 3.5 times as many high-quality events as a template matching-based catalogue. All events in the previous catalogue are identified with similar epicenters, depths, and magnitudes, while no false detections are found by visual inspection.

1. Introduction

Earthquake detection and location is one of the most fundamental tasks in seismology. Detailed understanding of the spatiotemporal distribution of seismicity is critical to the success of many research efforts in seismology and geophysics. A good algorithm for earthquake detection and location should be accurate, comprehensive, and efficient; ideally, the process should be entirely automated without human intervention.

Traditional earthquake location methods determine the best solution by minimizing travel time residuals at multiple stations. It is often an iterative, linearized process along the spatial and temporal gradients of the theoretical travel time predicted with an average velocity model (e.g., Eaton, 1970; Lee & Lahr, 1975; Herrmann, 1979). Although this strategy is computationally efficient, its accuracy depends largely on two factors. First, the phase picking must be done with caution to prevent mapping phase reading errors to hypocentral mislocation. Second, a velocity model that closely approximates true velocities in the subsurface is required to provide the travel time table and its gradients. It sometimes leads to a local rather than the global minimum when the first guess is far from the real hypocenter.

Grid search-based methods, such as the QUAKE3D (Nelson & Vidale, 1990) and the NonLinLoc (Lomax et al., 2000), have been developed to ensure that the best solution corresponds to the global minimum of travel time residuals. Using three-dimensional (3-D) velocity models in the calculation of theoretical travel times can also reduce errors due to structural heterogeneities (e.g., Nelson & Vidale, 1990; Wittlinger et al., 1993). Unfortunately, methods that directly depend on travel time residuals all suffer from three shortcomings: inaccurate velocity models, false phase picks, and trade-offs between the event location and origin time.

Using a totally different approach, Zhou (1994) developed the master station method that relies on travel time differences between a given master station and the rest of the seismic network to define the equal differential time (EDT) surfaces. The location where the greatest number of EDT surfaces intersect is deemed the hypocenter. This method successfully avoids the trade-off problem because it does not determine the original time and the hypocenter at the same time. It was further improved by Font et al. (2004) in establishing EDT surfaces for all possible station pairs. The improved method, named the maximum intersection (MAXI) method, can achieve high accuracy in spite of false picks and an imperfect velocity model.

All aforementioned location methods depend on phase picking that is usually performed by analysts through visual inspection. However, manual phase picking inevitably suffers from human errors and/or biases, and

its capacity is limited by available time and resources. The capacity issue is especially prominent in the studies of aftershock sequences of major earthquakes or induced seismicity during hydraulic fracturing, when hundreds of events may occur within hours (e.g., Eaton, 2018). To address this situation, automated techniques have been developed to perform phase picking based on characteristic functions such as the short-term-average and long-term-average ratio (e.g., Akram & Eaton, 2016; Allen, 1978, 1982; Baer & Kradolfer, 1987) or kurtosis (e.g., Küperkoch et al., 2010; Baillard et al., 2014). In general, a kurtosis-based approach performs better than short-term-average and long-term-average ratio but still misses $\sim 30\%$ of the manual picks (Baillard et al., 2014). A different strategy is to use neural networks to mimic the manual process (e.g., Dai & MacBeth, 1997; Perol et al., 2018; Wang & Teng, 1997). The most recently developed convolutional neural network is capable of identifying all events picked by visual inspection; however, it still gives some false alarms, and the event location accuracy is sometimes unsatisfactory (Perol et al., 2018; Ross et al., 2018). Moreover, it requires a good training data set which is not always available.

Another group of automatic detection and location methods was developed in the past two decades that requires no phase picking at all, including the source scanning algorithm (SSA) and its variants (Kao & Shan, 2004; Liao et al., 2012) and the waveform cross correlation-based template matching method (e.g., Bostock et al., 2012). The SSA searches possible events in all time and space and is ideal for difficult situations when phase identification and association become ambiguous. At each time, the stacked array energy has a 3-D distribution that is used to identify events. However, such a distribution always gives rise to a volume of highly possible hypocenters rather than a point source. It also leads to a trade-off issue between the sensitivity of event detection and the likelihood of false alarms. In comparison, the template matching technique depends on the similarity between seismogram pairs to detect events and uses differential times obtained by cross correlation to locate them. Therefore, it is most appropriate for detecting repeated and nearby events. Perol et al. (2018) show that template matching methods can miss $\sim 20\%$ of events compared to a manually produced catalogue.

In this study, we propose a novel algorithm that is capable of delineating extremely complicated spatiotemporal distributions of seismicity. This innovative method, named Seismicity-Scanning based on Navigated Automatic Phase-picking (S-SNAP), takes a cocktail approach that combines the advantages of three processes to automatically and comprehensively locate all seismic sources in a predefined model space with high accuracy and efficiency. We apply S-SNAP to a data set recorded by a dense local seismic array during a hydraulic fracturing operation to test this novel approach and to demonstrate the advantages of S-SNAP over conventional methods.

2. Method

S-SNAP consists of four major processes (Figure 1). The first one, preliminary source scanning, is adopted from the improved SSA (Liao et al., 2012), which searches for seismic sources by considering every possible location and time combination. Results of the preliminary source scanning are then used next to navigate the process of P and S phase picking within a confined segment of seismogram. The second process, phase picking, is a simplified version of the kurtosis-based P and S phase pickers (Baillard et al., 2014), which determines the precise onset time within the specified seismogram segment. The precisely determined P and S arrival times are used in the third process to locate earthquakes using an improved MAXI method (Font et al., 2004), which achieves high accuracy and reliability by allowing tolerances to some false picks and an imperfect velocity model. In the final process, the averaged moment magnitude (M_w) is determined from the distance-corrected Fourier spectra of seismic waveforms recorded at individual stations (Atkinson et al., 2008; Boore, 2003).

2.1. Preliminary Source Scanning

The basic idea of source scanning is to assume every grid node in a study area to be a potential source at any time. With a velocity model, the travel time from grid node i to station j can be calculated as tt_{ij} . Assuming that the origin time is t , then for a potential source i , its signal is expected to arrive at station j around the predicted arrival time $t + tt_{ij}$. By stacking all of the N stations' seismogram segments around $t + tt_{ij}$ and calculating the average energy of the stacked trace, the brightness as a function of grid node i and time t is defined as

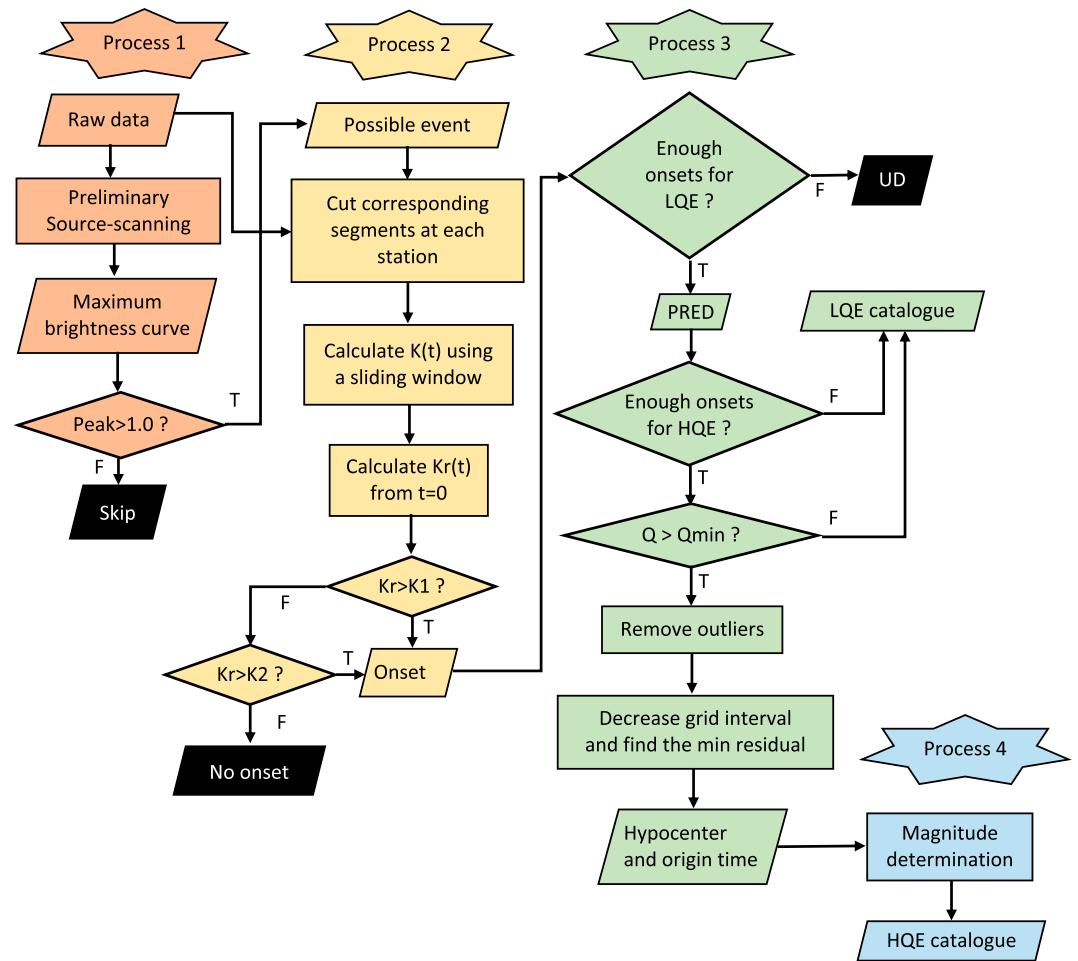


Figure 1. The flow chart for Seismicity-Scanning based on Navigated Automatic Phase-picking. Process 1 is preliminary source scanning, Process 2 is kurtosis-based phase picking, Process 3 is locating the source via intersection of equal differential time layers and travel time residuals, and Process 4 is magnitude determination. HQE, LQE, and UD stand for high-quality event, low-quality event, and unclear detection, respectively. K and Kr are kurtosis and kurtosis rate. And K1 and K2 are two Kr thresholds for phase picking. PRED is the preliminary solution determined by maximum intersection of EDT layers. Q is event quality, defined as the percentage of layers that intersect at the PRED, while Qmin is the quality threshold for high-quality events.

$$br(i, t) = \frac{1}{N} \sqrt{\frac{1}{win} \sum_{k=1}^{win} S_{it}^2(k)} \quad (1)$$

and

$$S_{it}(k) = \sum_{j=1}^N |s_j(t + tt_{ij} + (k - \frac{1}{4}win) \times \Delta t)|, \quad (2)$$

where $k \in (1, win)$, win is the number of sample points in a waveform segment, Δt is the sampling time interval, and S is the stacked amplitude from individual seismograms s after alignment with the assumed source location and time. If the assumed location and time correspond to a true seismic source, the brightness value is expected to reach a peak in both time and space domains. Otherwise, it yields a lesser value indicating noise.

This direct linear stacking suffers from several problems. First, because the brightness function depends on the amplitude of seismic signals, large amplitudes from nonsource effects can significantly contaminate the scanning result. For example, different signal-to-noise ratios (SNRs) and absolute amplitudes at different stations tend to skew individual stations' brightness contributions that in turn bias the brightness value.

Second, segments with extremely large amplitudes may overwhelm the brightness calculation regardless of whether or not the assumed location and time is correct, thus giving rise to artifacts. Finally, the background noise level often varies with time and is inevitably included in the brightness calculation, which means that the brightness threshold for identifying a seismic source may also vary with time.

We introduce two data processing schemes to overcome these problems. We first subdivide the continuous seismogram into 1-min segments and use the median amplitude as the representative noise level of that station within that minute. The individual minute-long segments are then normalized against these median amplitudes such that the normalized noise level of any station is ~ 1 at any time. The choice of 1-min duration for each segment is not critical and can vary depending on the expected total length of the earthquake signals, as long as a uniform noise amplitude of ~ 1 is achieved. Second, we take the third root to the seismograms to suppress anomalously large amplitudes that are clearly unrelated to source signals. As a result, the brightness function is redefined as

$$br(i, t) = \left[\frac{1}{N} \sqrt[3]{\frac{1}{win} \sum_{k=1}^{win} S_{it}^2(k)} \right]^3, \quad (3)$$

$$S_{it}(k) = \sum_{j=1}^N \left[\frac{|s_j(t + tt_{ij} + (k - \frac{1}{4}win) \times \Delta t)|}{\text{median}} \right]^{\frac{1}{3}}. \quad (4)$$

This revised approach ensures that every station has nearly equal weighting in the stacking process, yet stations with higher SNR can contribute more to the brightness function. Meanwhile, it can successfully reduce the influence of anomalously large nonsource amplitudes on the brightness calculation. Another benefit is that the roughly constant noise level requires only a single brightness threshold to identify the existence of seismic sources regardless of time.

Following Liao et al. (2012), we process waveform components including P and S phases independently and the final brightness function is given by

$$br = br_P \times br_S, \quad (5)$$

where br_P and br_S are brightness functions calculated based on P and S travel time tables, respectively.

During the implementation of our method, we take a scanning increment much larger than the sampling time interval to save calculation time. Consequently, t in equation (3) becomes stepwise. In each time step, a 3-D brightness distribution is determined and the maximum value is found. Those maximum values form a curve as a function of time. The peaks on that curve above a preset threshold indicate potential events. Based on each potential event's time and location, the waveform segments at individual stations that contain P or S onset are extracted and used in the next stage to navigate the phase picking process (Figure 1, Processes 1 and 2).

Although we have taken actions to suppress artifacts, false detections are inevitable when a low brightness threshold (e.g., 1.0, which actually represents the noise level) is used to identify as many potential events as possible. As the trade-off between brightness threshold and false alarm rate is a fundamental issue of SSA, a better strategy is to include as many potential events as possible in the preliminary scanning stage. We depend on the following two processes to address the problem of false detections.

2.2. Kurtosis-Based Phase Picking

On seismograms, both P and S phases may be recorded in all components. Rather than distinguish P and S onsets and deal with cross-contamination, we adopt Process 1's preliminary scanning results to ensure that there is only one onset within each time segment cut out from the continuous seismogram, which is already known to be either the P or S arrival of a particular earthquake. Therefore, the task here is much easier than the general problem of seismic phase detection. The characteristic function of kurtosis is chosen to deal with this simple situation. Kurtosis is defined as the fourth standardized moment of a group of sample points X :

$$K = \frac{E[(X - \mu)^4]}{E[(X - \mu)^2]^2}, \quad (6)$$

where μ is the mean value of X and E denotes the expectation. The kurtosis of a normally distributed data set is 3. Therefore, a window of seismogram including only Gaussian noise results in $K \approx 3$. On the other hand, the first m points of a seismic onset would break the normal distribution of a sample consisting of M points, giving the maximum kurtosis, while including a longer part of a signal lowers K . Therefore, two strategies can be applied to assign the onset time: Find a sudden rise or find the maximum value of K (Figure 1, Process 2). For convenience, we subtract 3 from the kurtosis values so that the noise gives ~ 0 .

We apply a short sliding window ($win_K = 1$ s) but containing enough sample points (e.g., 500) and move it one sample point each time on the segment to get the kurtosis value of that segment as a function of time, namely, $K(t)$. Then, the kurtosis rate is defined as

$$Kr(t) = K(t + dt) - K(t). \quad (7)$$

We first look for an obvious sudden rise from the beginning of the segment. If there is a time step t_0 where $Kr(t)$ reaches a preset threshold K_1 , the process stops, and we assign t_0 to be the onset time. If no such time step occurs throughout the entire segment, we then look for the maximum value of $Kr(t)$ and check whether it is larger than another preset threshold K_2 . If it is larger, the end time of that step minus the time duration of m sample points is assigned to be the onset time. If the two strategies both failed, then no pick is determined, meaning that the entire segment is considered random noise. We note that dt , K_1 , K_2 , and m are related to data quality, window duration, and sampling rate. Usually for a given data set, their values are fixed.

At the end of this process, we use the total number of picks to classify each event's overall quality into three groups: high-quality events (HQEs), low-quality events (LQEs), and unclear detections (UDs; Figure 1, Process 2).

In most cases, picks are reliable, but occasionally false picks are obtained. The reason could be an unexpected disturbance before the onset or that two onsets are so close to each other (e.g., ≤ 0.5 s) that they are included in one seismogram segment. This problem is addressed in the next process.

2.3. Locating the Source via EDT Layers and Travel Time Residuals

In this process, we adopt the MAXI method and determine the hypocenter of a seismic source in three steps. First, we use the arrival times of P and S phases obtained in the previous process to construct the EDT surfaces. Then we set a tolerance level of time error $Terr$, which would expand the EDT surface on both sides into an EDT layer. The grid node with the largest number of intersecting EDT layers is assigned the preliminary hypocenter solution (PRED). For each event with $n_P P$ picks and $n_S S$ picks, the maximum number of intersection of EDT layers at a grid node is

$$MAXI_{\text{ceil}} = \frac{n_P \times (n_P - 1)}{2} + \frac{n_S \times (n_S - 1)}{2}. \quad (8)$$

The quality value is defined as the actual number of EDT layers N_{EDT} divided by $MAXI_{\text{ceil}}$:

$$Q = \frac{N_{\text{EDT}}}{MAXI_{\text{ceil}}}. \quad (9)$$

If Q is smaller than a preset threshold Q_{min} , the event is deemed a LQE despite enough picks being obtained in the previous process. For a LQE, the PRED is considered the final solution.

For HQEs, a final step is performed with progressively finer grids to search iteratively for the minimum average residual between observed and theoretical arrival times. The final solution is declared when the preset finest grid (at the spacing interval of s) is reached or when the decrease of the average residual is negligible (i.e., below $p\%$).

One of the biggest advantages of using EDT layers for source location is that phase picks with anomalously large time residuals ($> t_{\text{out}}$), either due to false picking or other unknown reasons, form outliers that will have no influence (in relation to the majority of well-behaved picks) in the determination of the PRED. As they will not be used in the final solution, erroneous phase picks cannot contaminate the precision and accuracy of the event's location.

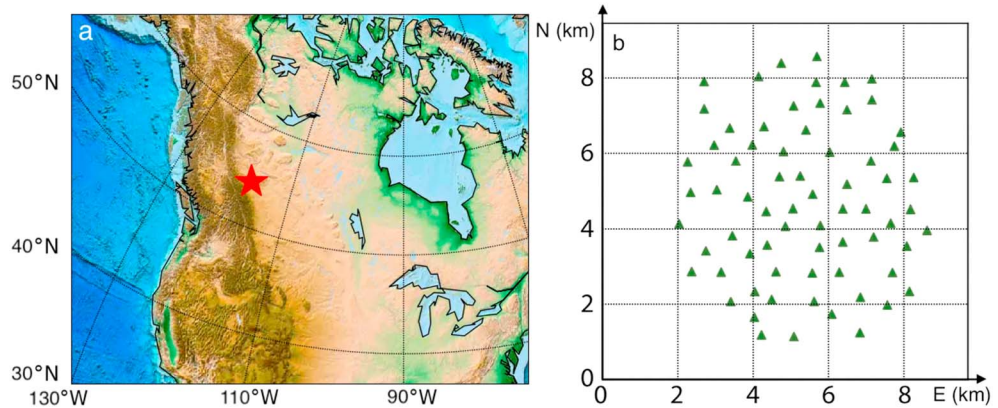


Figure 2. (a) Location of the Tony Creek Dual Microseismic Experiment program. The red star shows the location of the array in western Canada. (b) Detailed station distribution (green triangles) of the Tony Creek Dual Microseismic Experiment program.

2.4. Magnitude Determination

Detailed explanations of how Fourier spectra can be used to obtain the moment magnitude of an earthquake are available in Boore (2003) and Atkinson et al. (2008). Here we only provide the formulas for the purpose of reference and completeness. The seismic moment is derived by

$$M_0 = \frac{FD}{C}, \tag{10}$$

where FD is the median value of Fourier displacements at all stations corrected to $r_0 = 1$ km, and

Process	Description of parameter	Sign in this paper	Value and unit
Preliminary source scanning	Root before stacking		3 (T)
	Scanning window duration	win	1 s (T)
	Scanning increment		0.5 s (T)
	Scanning grid cell size		250 m (T)
	Detection threshold		1.0
Kurtosis-based phase picking	Kurtosis calculation window	win_K	1 s
		dt	5 Sample points
	Kr Threshold 1	K_1	3
	Kr Threshold 2	K_2	1 (T)
MAXI-EDT source location		m	10 Sample points
	Threshold for LQE		4 (T)
	Threshold for HQE		15 (T)
		$Terr$	0.1 s (T)
	Minimum Q for HQE	$Qmin$	0.5
		t_{out}	0.5 s (T)
Magnitude determination		s	1 m (T)
		p	0.1
		R	0.55
		v	0.71
		F	2

Note. Parameter values with “(T)” followed are set for the Tony Creek Dual Microseismic Experiment data set and may need to be changed for data sets with differing characteristics. HQE = high-quality events; LQE = low-quality events; MAXI = maximum intersection; EDT = equal differential time.

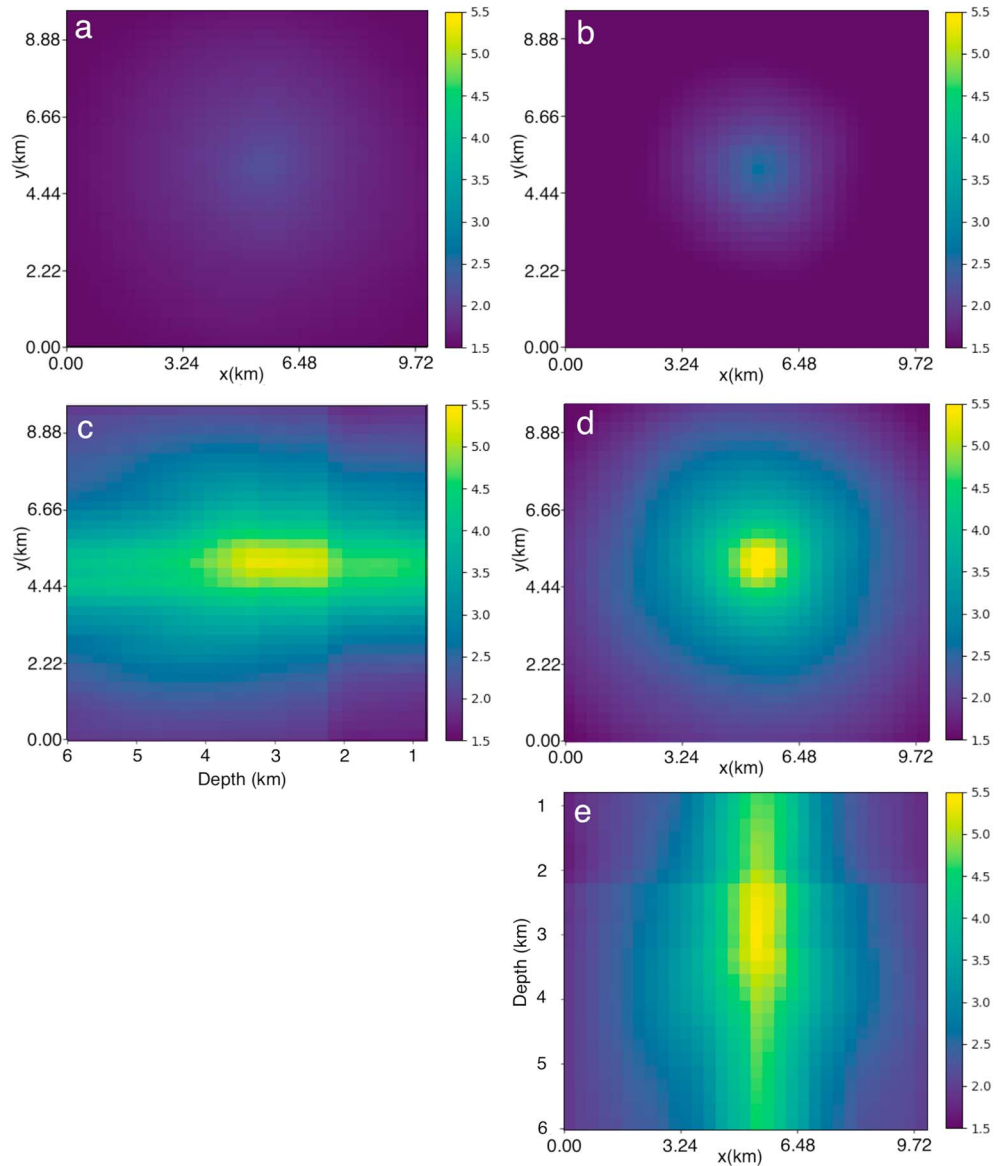


Figure 3. Slices including the maximum value of 3-D brightness map in the 36th step (18 s) in H1. (a) Top view of P brightness map. (b) Top view of S brightness map. (c–e) Left view, top view, and front view of combined brightness map.

$$C = \frac{RvF}{4\pi\rho r_0\beta^3} \times 10^{-20}, \quad (11)$$

where ρ is the density of the source material in grams per cubic centimeter, β is the shear wave velocity in kilometer per second, $R = 0.55$, $v = 0.71$, and $F = 2$. The moment magnitude is calculated from the correspond moment following Hanks and Kanamori (1979):

$$M_w = \frac{2}{3} \log_{10} M_0 - 10.71, \quad (12)$$

where M_0 is expressed in dyne centimeters. This process is also totally automatic.

3. Application to Induced Seismicity Data

We apply S-SNAP to data from the Tony Creek Dual Microseismic Experiment (ToC2ME), a passive seismic monitoring program that recorded induced seismicity from a four-well hydraulic-fracturing operation

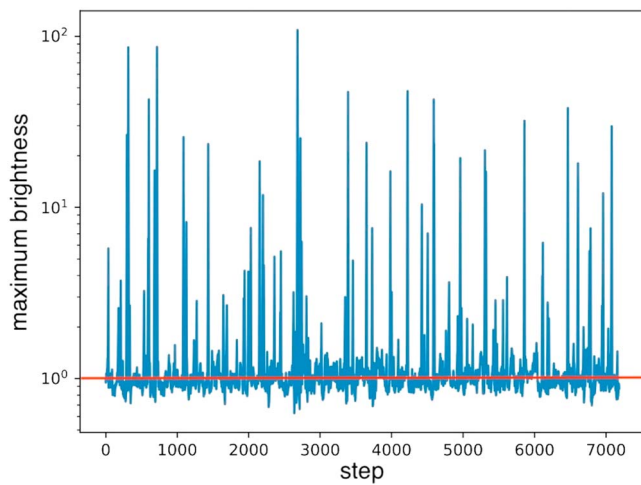


Figure 4. Maximum brightness curve for H1. One step is 0.5 s. All peaks above 1.0 (red line) are considered potential events, entering Process 2.

in Alberta, Canada (Eaton et al., 2018). Sixty-eight three-component geophones were installed in shallow wellbores and an accelerometer was installed near the surface (Figure 2), all with a sampling rate of 500 Hz. A detailed one-dimensional velocity model for both P and S waves is available for the area based on well logs to a depth of 3.5 km and crustal refraction profiles below that (Zelt & Ellis, 1989). For the purpose of illustrating the merits of our method, we select 3 hr of continuous waveform data with distinctive features. In the busiest hour (H1, Hour 20 of 5 November), 40 events were identified in the ToC2ME catalogue (Eaton et al., 2018). In the second hour (H2, Hour 14 of 27 November), two large earthquakes ($M_w > 1$) and three smaller ones were identified. In contrast, the third hour (H3, Hour 8 of 1 November) provides no event in the ToC2ME catalogue. Results of H1 will be discussed first, followed by the other two.

In the first preliminary scanning process, we set the search volume to be a cuboid below the seismic array with a grid interval of ~ 250 m. We precalculate the P and S waves travel times for each grid node-station pair using the software “TauP” (Crotwell et al., 1999). Table 1 summarizes parameters in all processes of S-SNAP and corresponding values used in processing ToC2ME data set.

Given the station distribution, P waves mainly excite the vertical component, while S waves mainly excite horizontal components. Thus, we apply the P and S travel time tables to the vertical and horizontal components, respectively. In each time step, we determine 3-D brightness distributions for P and S waves separately, and the combined results are used to identify the grid node with the maximum brightness (equation (5) and Figure 3). After the entire hour is scanned, we plot each maximum brightness value as a function of time (Figure 4) and take all peaks with brightness value > 1.0 (488 in total) as potential events entering the next process. Some of these events are located close to injection wells, as the example shown in Figure 3, but many others are scattered across the study area. Possible reasons for mislocation in this process include the misalignment of seismogram segments, low SNRs of the waveform data, and false detections due to contamination of large random noise, as the examples shown in Figure 5.

The second process, kurtosis-based phase picking, is highly effective in eliminating false detections. We use the average onset time determined from the two horizontal components to be the S arrival. In the case that the onset time can be determined from only one horizontal component, it is taken as the corresponding S arrival time. We define an HQE as having at least 15 P and 15 S arrivals. Similarly, an LQE has 4–14 P or 4–14 S arrivals. Otherwise, the event is classified in the UD category (Figure 5). In total, we have found 125 HQEs, 143 LQEs, and 220 UDs in H1 (Table 2).

By demanding the quality value Q (equation (9)) to be at least 0.5 for HQEs in the next process of locating events with the MAXI method, two events are downgraded from HQE to LQE (Table 2). This threshold for Q , meaning that $> 50\%$ of picks are used in the location process, is a logical choice and could be used in other data sets. In searching the final solutions, we set the smallest grid interval (s) and the residual improvement percentage (p) to be 1 m and 0.1, respectively. For most HQEs, the minimum residual can be obtained with a spatial resolution between 1 and 10 m. The average and median values of travel time residual for all 123 HQEs are both 0.04 s. The 3-D distribution of HQE hypocenters is shown in Figure 6. They concentrate in a small area surrounding the injection wells with a linear NE-SW trending pattern. Their depths fall in a narrow range around 3,250 m, which is ~ 200 m above the hydraulic fracturing depth of about 3,445 m. However, the sharp vertical alignment of the events is due to a discontinuity in the velocity model.

The 3-D distributions of HQE hypocenters during H2 and H3 are also presented in Figure 6. The focal depths of all these events are remarkably consistent with the results for H1. The hypocenters are all located near the wells but with linear patterns different from the one identified for H1, probably corresponding to different fault systems. The numbers of events with each quality category are summarized in Table 2 for all three selected hours.

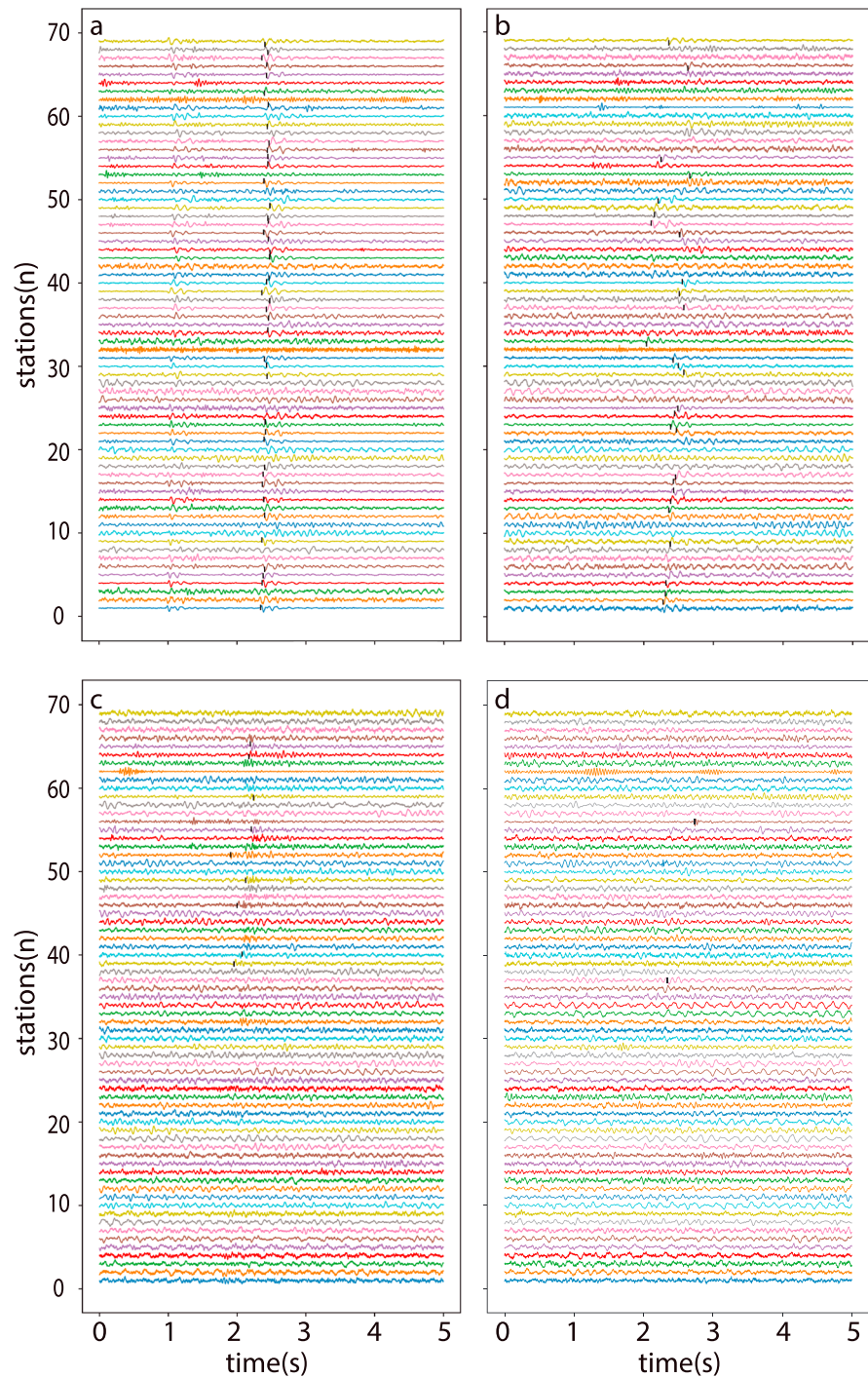


Figure 5. Phase picking examples. (a) S_2 picks of a well-aligned high-quality event (HQE; H1, step 179). The event about 1.4 s before is also identified as another well-aligned HQE. (b) S_1 picks of a poorly aligned HQE (H1, step 216). (c): P picks of a low-quality event (H1, step 89). (d) P picks of an unclear detection (H1, step 13).

For M_w determination, we read ρ and β from the velocity model according to the event depth. The results are also summarized in Table 2.

In general, the performance of S-SNAP is stable and consistent regardless of the number of events in each hour or the magnitude range. Taking H1, for example, we have obtained 268 solutions (123 HQEs and 145 LQEs), equivalent to one event every 13 s on average. For H2 and H3, the average occurrence rate is one event per 39 and 28 s, respectively. Magnitudes in H1 range between -0.21 and 0.33 . There are two relatively

Table 2
Summarized Results for All 3 hr

Hour	HQE(P2/F)	LQE(P2/F)	UD	Total	M_w range (HQE)
H1	125/123	143/145	220	488	-0.21 to 0.33
H2	19/19	74/74	494	587	-0.15 to 1.72
H3	17/17	111/111	470	598	-0.14 to 0.01

Note. “P2” means results in “Process 2,” while “F” means final results. HQE, LQE, and UD stand for high-quality event, low-quality event, and unclear detection, respectively.

large events in H2 with M_w of 1.72 and 1.01. In H3, there is no event larger than M_w 0.01. We have verified all HQEs by visually examining their waveform segments, and this confirms that no false detections occurred.

4. Discussion

The advantage of S-SNAP can be summarized in two aspects: (1) The process is completely automated and highly efficient, and (2) the result is accurate, consistent, and comprehensive. Because no human intervention is required during the entire process, the S-SNAP result does not suffer from any interpreter bias. The processing time depends largely on numbers of stations and grid nodes in the study area. With 69 stations and 29,295 grid nodes, it takes less than 3 hr to process the busiest hour (H1, Table 2) with 123 HQEs out of more than 480 detections on a standard laptop computer. By using parallel computing, it is easy to run S-SNAP in near-real-time mode for automatic earthquake monitoring and precise location or to process very long duration continuous data (e.g., 1 year) for an area of interest.

We compare our results with the seismicity catalogue obtained by the original ToC2ME study (D. W. Eaton et al., 2018) to further illustrate the advantages of S-SNAP (Table 3). The ToC2ME catalogue was obtained

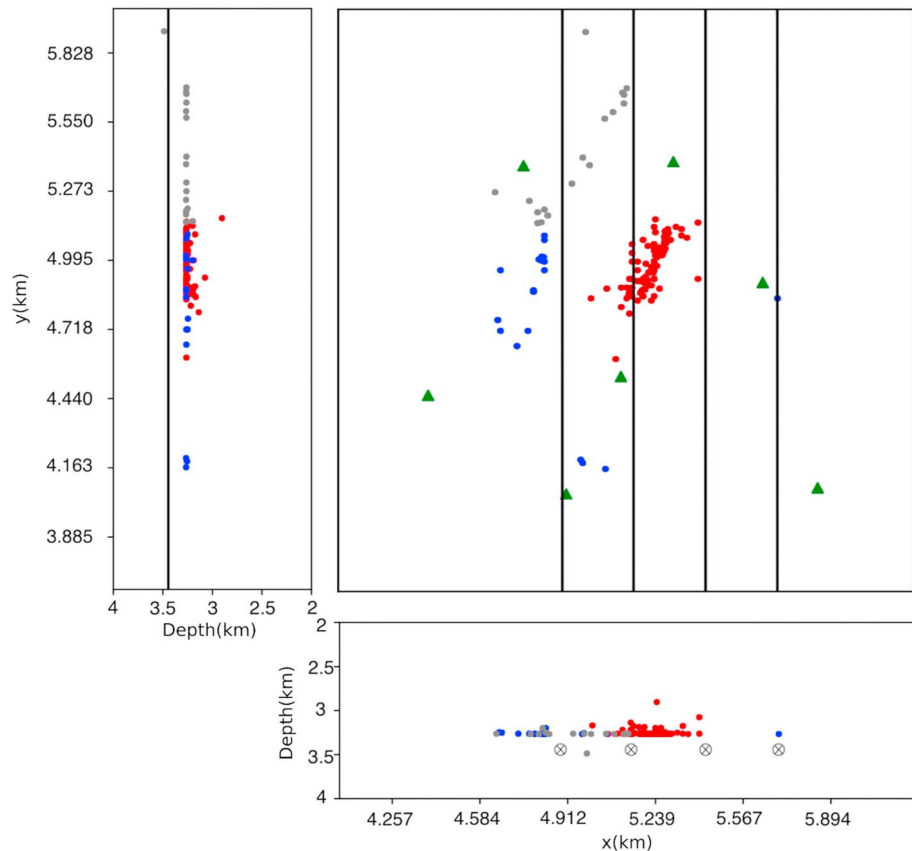


Figure 6. HQE locations for H1 (red), H2 (blue), and H3 (gray). Black lines and quartered circles show the locations and depth of the horizontal injection wells. Green triangles are stations.

Table 3
Comparison Between S-SNAP and ToC2ME Catalogues for All 3 hr

Hour	Absolute time	Class	S-SNAP	ToC2ME
H1	5 Nov., Hour 20	HQE	123	40
		LQE	145	108
		UD	220	44
		Total	488	192
H2	27 Nov., Hour 14	HQE	19	5
		LQE	74	23
		UD	494	24
		Total	587	52
H3	1 Nov., Hour 8	HQE	17	0
		LQE	111	19
		UD	470	26
		Total	598	45

Note. S-SNAP = Seismicity-Scanning based on Navigated Automatic Phase-picking; ToC2ME = Tony Creek Dual Microseismic Experiment; HQE = high-quality event; LQE = low-quality event; UD = unclear detection.

using a template matching method and verified by visual inspection and is thus considered free from spurious events. It is very encouraging that all HQEs in the ToC2ME catalogue are included in the S-SNAP catalogue with similar original times and epicenters. The M_w values between the two catalogues are very consistent for events with $M_w = 0.2$ or larger, while smaller events appear to show more scatter. In terms of focal depth, the S-SNAP results are more concentrated (Figure 6), which we interpret as being more consistent.

Overall, S-SNAP found about 3.5 times as many HQEs as ToC2ME (159 events vs. 45 events, Table 3). Taking the numbers of HQE and LQE together, our catalogue has about 2.5 times as many events as the ToC2ME catalogue (489 events vs. 195 events, Table 3). Given the almost identical definition of HQE (at least 15 stations recording both P and S arrivals are required in the ToC2ME catalogue, while our threshold is 15 P phase and 15 S phase picks), these numbers demonstrate that S-SNAP can be a powerful tool for delineating the detailed spatiotemporal distribution of induced seismicity in the vicinity of injection sites. In addition, this disparity of event numbers may be caused by template bias in the ToC2ME catalogue, which in turn reflects one of the advantages of S-SNAP that every event is independent, so that it can provide a more comprehensive catalogue.

Table 4
Comparison Among Different Station Numbers Using H1 Data

Number of stations	HQE numbers	Threshold	Max diff (m)	Mean diff (m)
69	123	15		
69	134	10		
35	113	10	209	50
23	93	10	391	57
14	80	7	412	101
7	61	5	567	124
69 (ToC2ME)	40	15		

Note. Threshold means the minimum number of P and S arrivals picked to be an HQE. The abbreviation “diff” means hypocentral difference, defined as the distance between the hypocenter determined by all 69 stations (Seismicity-Scanning based on Navigated Automatic Phase-picking catalogue) and that by fewer stations. HQE = high-quality event; ToC2ME = Tony Creek Dual Microseismic Experiment.

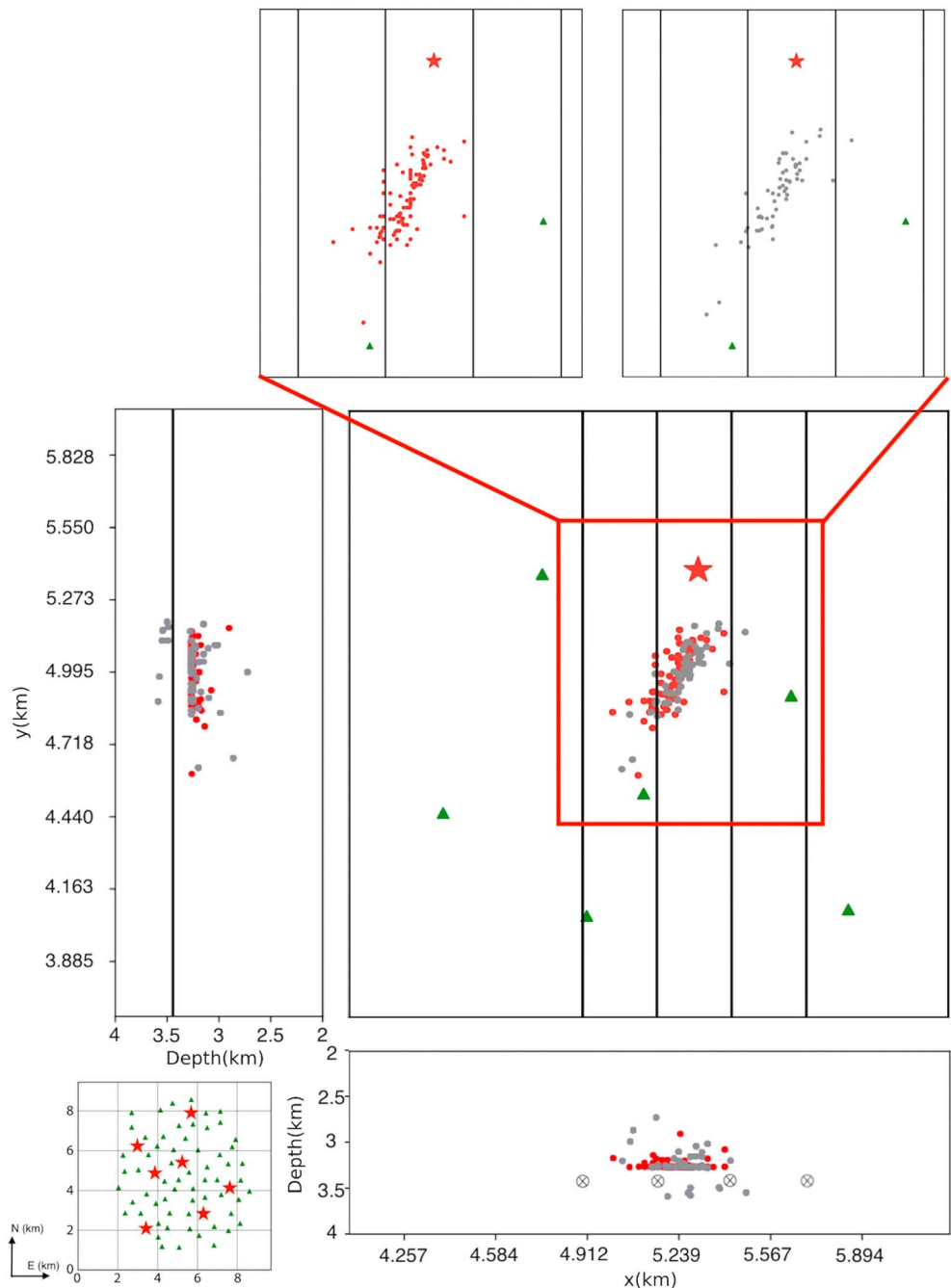


Figure 7. High-quality event locations by 7 stations with at least 5 *P* and 5 *S* picks (gray dots) and 69 stations with at least 15 *P* and 15 *S* picks (red dots) for H1. Black lines and quartered circles show the locations and depth of the horizontal injection wells. Red stars show seven selected stations, while the remaining unused stations are represented by green triangles.

The uncertainty of the final location depends on the accuracies of phase picking and the velocity model. In this study, the travel time residual of all HQEs is 0.04 s on average, corresponding to approximately 200–250 m in distance. This is much larger than the final grid interval used in Process 3. Nevertheless, it is probably necessary to make the grid interval smaller than the spatial uncertainty in order to obtain the most accurate solutions.

We acknowledge that seismic station coverage as dense as the ToC2ME array is extraordinary and unavailable for most seismic experiments. To test the performance of S-SNAP with a sparser array, we repeat the

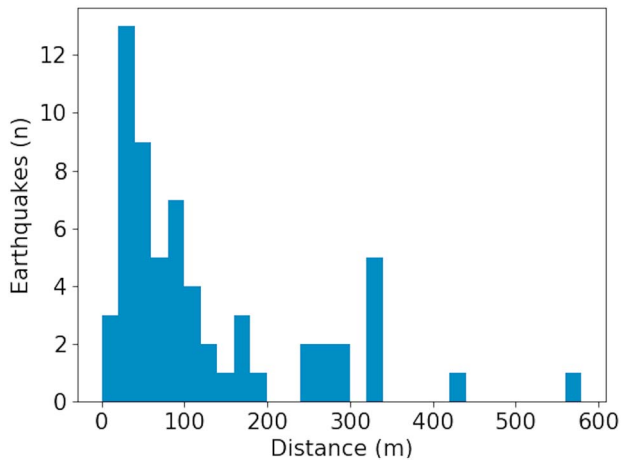


Figure 8. Histogram of hypocentral differences between locations derived by 7 stations and 69 stations.

location process using H1 data with decreasing numbers of stations (Table 4). As expected, the number of HQE solutions decreases with fewer stations. However, even with only seven stations (about one tenth of the available stations), S-SNAP still identifies 61 HQEs, which is ~50% more of that in the ToC2ME catalogue. A few events originally considered LQEs are now identified as HQEs because of the lower thresholds with fewer stations, and all of them are located within or near the event cluster.

We define the hypocentral difference as the distance between the hypocenter determined by all 69 stations (S-SNAP catalogue) and that by fewer stations. If a new event is detected, the original location is simply assumed to be at the center of the cluster. Our experiment results show that all HQE solutions are stable (hypocentral difference <600 m), and no false detections were produced by eliminating stations. Both the maximum and average hypocentral differences increase with fewer stations; however, the mean value is always much smaller than the estimated uncertainty of about 250 m.

Figure 7 shows the extreme example of using only seven stations. When compared to the results with all 69 stations, the linear pattern of epicenters remains unchanged and most solutions stay at the same depth (~3,250 m). The majority of the events have hypocentral differences of less than 150 m (Figure 8). These results demonstrate that, even with only one tenth of the total stations, S-SNAP can still perform reliably and produce a catalogue more comprehensive than the original ToC2ME catalogue with no false detections. More significantly, the required calculation time decreases dramatically by ~83% from ~3 hr to only ~30 min on the same laptop computer.

Ideally, the threshold for HQE should be set in such a way that the maximum number of events can be located with tolerable uncertainty and no false detections. When there are more than 30 stations, the result is not very sensitive to the threshold because the number of phase arrivals is often more than what is required to derive a stable solution for most events. As shown in Table 4, using 10 and 15 as the thresholds for 69 stations results in less than a 10% change in the number of HQE. However, with fewer than 20 stations, the threshold should be half of the total number of stations to ensure the solution quality. We find that a threshold of five stations is the lower limit for all cases. The empirical relationship between the choice of threshold for HQE and the total number of available stations is presented in Figure 9. We note that this threshold may depend on many other factors including SNR and array size. Thus, when applying S-SNAP to other data sets, visual inspection for a few testing hours might be necessary.

Similarly, we test the performance of S-SNAP with different scenarios of azimuthal gap. Figure 6 shows the result with the total 69 stations (at least one station every 15°). In a series of experiments, we use the H1 data and repeat the location process with stations located only on the northern side (azimuthal gap = 180°

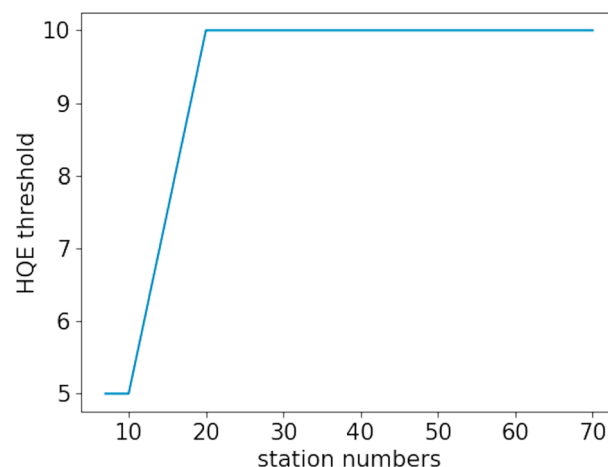


Figure 9. Recommended HQE threshold for different station numbers. HQE = high-quality event.

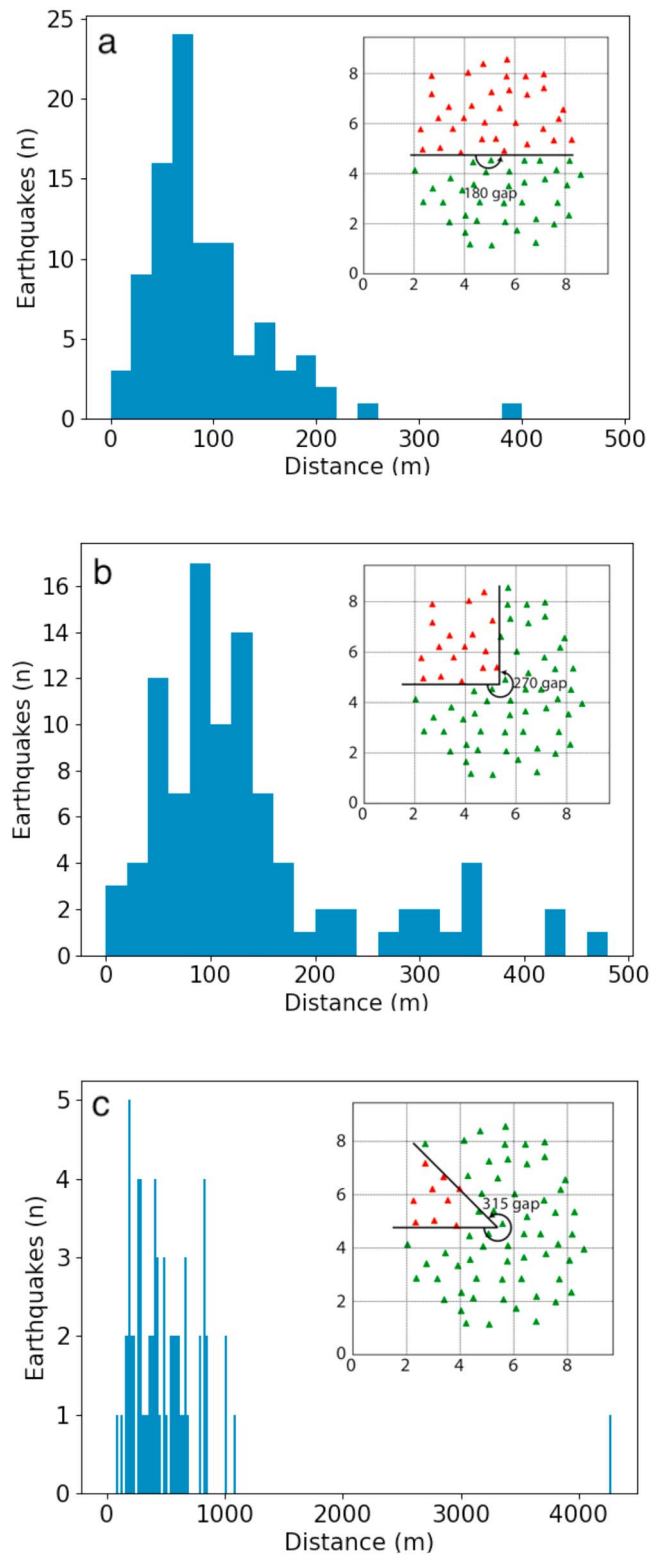


Figure 10. Station distributions for different azimuthal gaps and corresponding histograms of hypocentral difference compared with results from 69 stations. Green triangles represent all the stations, while red color highlights those used in each test. The width of each rectangle is 20 m.

, Figure 10a), in the northwestern quadrant (azimuthal gap = 270° , Figure 10b), and in the WNW octant (azimuthal gap = 315° , Figure 10c). When the results of 180° and 270° azimuthal gap are compared to the original catalogue, the average hypocentral difference is on the order of 100 m with the maximum less than 500 m. However, if the gap is as large as 315° , the worst event is mislocated by as much as 4 km and the mean difference increases to about 500 m, almost twice the original uncertainty. Thus, the upper limit of azimuthal gap for S-SNAP in this case is about 270° .

We note that the brightness threshold used in the preliminary scanning (i.e., Process 1) is important. In theory, the preliminary scanning results are more reliable when a higher threshold is used. The trade-off, however, is the increased possibility of missing events. On the other hand, if a lower threshold is used in Process 1, the results are more comprehensive but may contain many artifacts. In this study, we take the most conservative approach by setting it at 1.0, which is equivalent to the mean value of random noise. The main rationale for using this approach is that S-SNAP relies on the preliminary scanning (i.e., Process 1) to ensure the completeness of the catalogue. Because the issue of eliminating artifacts can be properly handled by subsequent processes, we recommend that this threshold should be set as low as reasonably possible. A higher brightness threshold can jeopardize the completeness of S-SNAP results.

Scanning increment, window duration and grid cell size also play important roles. The time window should be long enough to include the whole *P* or *S* wave train (in this case, less than 1 s for $M_w \leq 2$ earthquakes) and the tolerable error in travel time prediction due to inaccurate velocity model, whereas the increment should be smaller than the window duration. Shorter increments and durations lead to improved time resolution but at the risk of failure to correctly identify larger earthquakes with longer source time functions. The scanning parameters used in this study (1-s window and 0.5-s increment) are able to resolve two events that are only ~1.4 s apart in origin time. However, we note that such high time resolution may only be possible if the two events are comparable in size. In case that one of the events is much larger than the other, the brightness peak of the smaller one may be buried in the peak of the larger one, making it invisible to preliminary scanning. The scanning grid cell size should be as small as possible; however, it causes huge increase in computing time. So we recommend setting this parameter according to the computing capacity or decreasing it until the outcomes have only negligible changes.

We have conducted a number of experiments by taking the second, third, or fourth root to the input data before stacking. The results show that the second root is insufficient to diminish the dominance of spurious signals from some stations, while the fourth root sometimes suppresses true signals too harshly. However, different conclusions may be reached for different data sets (e.g., Muirhead & Datt, 1976; Xu et al., 2009). We also tried setting an upper limit for the data points so that any value exceeding that threshold is suppressed. However, this approach reduces the time resolution, and the issue of selecting the optimal threshold is difficult to determine a priori.

In the phase picking process, we calculate $Kr(t)$ with $dt = 5$ sample points. This value comes from the result of a series of experiments with dt ranging from 1 to 10. Our experiments show that $dt = 4, 5, \text{ or } 6$ all give similarly good results. Based on this, we found that $Kr(t)$ reaches a maximum 5 to 20 sample points after the onset in most cases. This is the main reason that we take $m = 10$ in our application. We suggest that dt and m can be fixed in applying S-SNAP to different data sets (Table 1). The $Kr(t)$ threshold K_2 depends on the SNR of the data set. While $K_1 = 3$ can pick out good signals, K_2 includes more possible onsets. In the high-quality ToC2ME data set, $K_2 = 1$ hardly adds any false positives. However, this value should be raised to 1.5 or 2 in noisier cases.

Parameters in Process 3, $Terr$ and t_{out} , can vary in different study areas with different data sets. If the epicentral distances become much larger or the velocity model is less accurate, the predicted travel time will consequently have a large uncertainty, and $Terr$ and t_{out} should be made larger to accommodate the possible errors. If $Terr$ is too small, fewer EDT layers could intersect at the hypocenter, causing a smaller N_{EDT} and a lower quality (Q , equation (9)). Therefore, when too many HQEs are downgraded to LQEs as a result of smaller Q , this is a clear sign of $Terr$ being too small. Also, multiple $Terr$ values could be used at the same time (Theunissen et al., 2012) to break the strong dependence on the single value.

Finally, we note that the size of the study region can affect the temporal resolution. Besides the grid nodes close to the real hypocenter, others are also possible to align some of the onsets with a different origin time and a smaller brightness value (equations (3) and (5)). This would flatten the peaks on the maximum bright-

ness curve (Figure 4) or even give multiple peaks for a single event, especially when a sufficiently large area (e.g., regional scale) is scanned. Consequently, smaller events right before or after a big event will become invisible. The effect depends on the size of the study area, the separation times and magnitude differences between events. When applying S-SNAP to a regional scale study, a lower temporal resolution and potential artifacts caused by multiple local brightness peaks for a single event should be considered. Application to other data sets may require modifications to the current S-SNAP workflow, which will be the focus of future work.

5. Conclusion and Future Works

The S-SNAP method successfully fulfills the objective of automatic earthquake location with the highest completeness and accuracy. The performance can also be efficient when it is implemented with a parallel-computing approach. Application to real seismic data collected during hydraulic fracturing operations has demonstrated S-SNAP's advantages in detecting and locating induced earthquakes that are clustered in both time and space. We plan to expand the application of S-SNAP to other problems challenging to most conventional methods, such as the determination of hypocenters of the extremely high number of aftershocks during the first few hours or days of a major earthquake or the detection of very small earthquakes in a noisy environment. The more comprehensive earthquake catalogues produced by S-SNAP can also provide greater insight for seismotectonic studies. They can also be used as a much better training set in many machine-learning applications to enhance the accuracy of model prediction.

Acknowledgments

We are grateful to the Associate Editor and two anonymous reviewers for their constructive comments. This study benefited from constructive discussions with Nadine Igonin, Byron Kontou, and Ryan Visser. We thank Connor Gaudreau for helping us develop the parallel-computing portion of the S-SNAP program used in this study. Our S-SNAP code in Python 3 is available on Github at <https://github.com/tanfengzhou/S-SNAP1.0.git>, along with the raw waveforms used in the study. Station locations and time are modified to avoid presenting proprietary information. Continuous raw data (geophone and broadband recordings, network code TC2ME) are available, following a holdback period that expires on 1 July 2020, through the Incorporated Research Institutions for Seismology (IRIS) data center (<http://ds.iris.edu/mda/5B?timewindow=2016-2017>). The Tony Creek Dual Microseismic Experiment (ToC2ME) program was enabled by generous support from two companies. The ToC2ME program was acquired using the BuriedArray method, under a licence from Microseismic Inc. This research was supported by the Natural Sciences and Engineering Research Council of Canada (NSERC) Discovery grants RGPIN/418268-2013 (H. K.) and 2017 04029 (E. N.), the Energy Innovation Program of Natural Resources Canada (H. K.), University of Victoria Graduate Fellowship (F. T.) and a Canada Research Chair (E. N.).

References

- Akram, J., & Eaton, D. W. (2016). A review and appraisal of arrival-time picking methods for downhole microseismic data. *Geophysics*, *81*(2), KS71–KS91.
- Allen, R. (1978). Automatic earthquake recognition and timing from single traces. *Bulletin of the Seismological Society of America*, *68*(5), 1521–1532.
- Allen, R. (1982). Automatic phase pickers: Their present use and future prospects. *Bulletin of the Seismological Society of America*, *72*(6B), S225–S242.
- Atkinson, G. M., Kaka, S. I., Eaton, D., Bent, A., Peci, V., & Halchuk, S. (2008). A very close look at a moderate earthquake near Sudbury, Ontario. *Seismological Research Letters*, *79*(1), 119–131.
- Baer, M., & Kradolfer, U. (1987). An automatic phase picker for local and teleseismic events. *Bulletin of the Seismological Society of America*, *77*(4), 1437–1445.
- Baillard, C., Crawford, W. C., Ballu, V., Hibert, C., & Mangeney, A. (2014). An automatic kurtosis-based P- and S-phase picker designed for local seismic networks. *Bulletin of the Seismological Society of America*, *104*, 394–409.
- Boore, D. M. (2003). Simulation of ground motion using the stochastic method. *Pure and Applied Geophysics*, *160*(3-4), 635–676.
- Bostock, M. G., Royer, A. A., Hearn, E. H., & Peacock, S. M. (2012). Low frequency earthquakes below southern Vancouver Island. *Geochemistry, Geophysics, Geosystems*, *13*, Q11007. <https://doi.org/10.1029/2012GC004391>
- Crotwell, H. P., Owens, T. J., & Ritsema, J. (1999). The TauP Toolkit: Flexible seismic travel-time and ray-path utilities. *Seismological Research Letters*, *70*(2), 154–160.
- Dai, H., & MacBeth, C. (1997). The application of back-propagation neural network to automatic picking seismic arrivals from single-component recordings. *Journal of Geophysical Research*, *102*(B7), 15,105–15,113.
- Eaton, J. P. (1970). HYPOLAYR, a computer program for determining hypocenters of local earthquakes in an earth consisting of uniform flat layers over a half space (69-85). U.S. Geological Survey.
- Eaton, D. W. (2018). *Passive seismic monitoring of induced seismicity: Fundamental principles and application to energy technologies*. Cambridge: Cambridge University Press.
- Eaton, D. W., Igonin, N., Poulin, A., Weir, R., Zhang, H., Pellegrino, S., & Rodriguez, G. (2018). Induced seismicity characterization during hydraulic-fracture monitoring with a shallow-wellbore geophone array and broadband sensors. *Seismological Research Letters*, *89*, 1641–1651.
- Font, Y., Kao, H., Lallemand, S., Liu, C.-S., & Chiao, L.-Y. (2004). Hypocentre determination offshore of eastern Taiwan using the maximum intersection method. *Geophysical Journal International*, *158*(2), 655–675.
- Hanks, T. C., & Kanamori, H. (1979). A moment magnitude scale. *Journal of Geophysical Research*, *84*(B5), 2348–2350.
- Herrmann, R. B. (1979). Fasthypo—A hypocenter location program. *Seismological Research Letters*, *50*(2), 25–38.
- Kao, H., & Shan, S.-J. (2004). The source-scanning algorithm: Mapping the distribution of seismic sources in time and space. *Geophysical Journal International*, *157*(2), 589–594.
- Küperkoch, L., Meier, T., Lee, J., & Friederich, W. (2010). Automated determination of P-phase arrival times at regional and local distances using higher order statistics. *Geophysical Journal International*, *181*(2), 1159–1170.
- Lee, W. H., & Lahr, J. C. (1975). HYP071 (revised); a computer program for determining hypocenter, magnitude, and first motion pattern of local earthquakes: U.S. Dept. of the Interior, Geological Survey, National Center for Earthquake Research.
- Liao, Y., Kao, H., Rosenberger, A., Hsu, S., & Huang, B. (2012). Delineating complex spatiotemporal distribution of earthquake aftershocks: An improved Source-Scanning Algorithm. *Geophysical Journal International*, *189*(3), 1753–1770.
- Lomax, A., Virieux, J., Volant, P., & Berge-Thierry, C. (2000). Probabilistic earthquake location in 3D and layered models. In C. H. Thurber & N. Rabinowitz (Eds.), *Advances in seismic event location, Modern Approaches in Geophysics* (pp. 101–134). Dordrecht, Netherlands: Springer.
- Muirhead, K. T., & Datt, R. (1976). The N-th root process applied to seismic array data. *Geophysical Journal of the Royal Astronomical Society*, *47*(1), 197–210.

- Nelson, G. D., & Vidale, J. E. (1990). Earthquake locations by 3-D finite-difference travel times. *Bulletin of the Seismological Society of America*, *80*(2), 395–410.
- Perol, T., Gharbi, M., & Denolle, M. (2018). Convolutional neural network for earthquake detection and location. *Science Advances*, *4*(2), e1700578.
- Ross, Z. E., Meier, M.-A., Hauksson, E., & Heaton, T. H. (2018). Generalized seismic phase detection with deep learning. *Bulletin of the Seismological Society of America*, *108*(5A), 2894–2901.
- Theunissen, T., Font, Y., Lallemand, S., & Gautier, S. (2012). Improvements of the maximum intersection method for 3D absolute earthquake locations. *Bulletin of the Seismological Society of America*, *102*(4), 1764–1785.
- Wang, J., & Teng, T.-l. (1997). Identification and picking of S phase using an artificial neural network. *Bulletin of the Seismological Society of America*, *87*(5), 1140–1149.
- Wittlinger, G., Herquel, G., & Nakache, T. (1993). Earthquake location in strongly heterogeneous media. *Geophysical Journal International*, *115*(3), 759–777.
- Xu, Y., Koper, K. D., Sufri, O., Zhu, L., & Hutko, A. R. (2009). Rupture imaging of the Mw 7.9 12 May 2008 Wenchuan earthquake from back projection of teleseismic P waves. *Geochemistry, Geophysics, Geosystems*, *10*, Q04006. <https://doi.org/10.1029/2008GC002335>
- Zelt, C. A., & Ellis, R. M. (1989). Seismic structure of the crust and upper mantle in the Peace River Arch Region, Canada. *Journal of Geophysical Research*, *94*(B5), 5729–5744.
- Zhou, H. (1994). Rapid three-dimensional hypocentral determination using a master station method. *Journal of Geophysical Research*, *99*, 15,439–15,455.